

# Realistic galaxy image simulation via score-based generative models

Michael J. Smith<sup>1,2\*</sup>, James E. Geach<sup>1,2</sup>, Ryan A. Jackson<sup>3</sup>, Nikhil Arora<sup>4</sup>, Connor Stone<sup>4</sup>  
and Stéphane Courteau<sup>4</sup>

<sup>1</sup>*Centre of Data Innovation Research, Department of Physics, Astronomy, and Mathematics, University of Hertfordshire, Hatfield, AL10 9AB*

<sup>2</sup>*Centre of Astrophysics Research, Department of Physics, Astronomy, and Mathematics, University of Hertfordshire, Hatfield, AL10 9AB*

<sup>3</sup>*Department of Astronomy and Yonsei University Observatory, Yonsei University, Seoul 03722, Republic of Korea*

<sup>4</sup>*Department of Physics, Engineering Physics, and Astronomy, Queen's University, Kingston, ON K7L 3N6, Canada*

1 February 2022

## ABSTRACT

We show that a Denoising Diffusion Probabilistic Model (DDPM), a class of score-based generative model, can be used to produce realistic mock images that mimic observations of galaxies. Our method is tested with Dark Energy Spectroscopic Instrument (DESI) *grz* imaging of galaxies from the Photometry and Rotation curve OBservations from Extragalactic Surveys (PROBES) sample and galaxies selected from the Sloan Digital Sky Survey. Subjectively, the generated galaxies are highly realistic when compared with samples from the real dataset. We quantify the similarity by borrowing from the deep generative learning literature, using the ‘Fréchet Inception Distance’ to test for subjective and morphological similarity. We also introduce the ‘Synthetic Galaxy Distance’ metric to compare the emergent physical properties (such as total magnitude, colour and half light radius) of a ground truth parent and synthesised child dataset. We argue that the DDPM approach produces sharper and more realistic images than other generative methods such as adversarial networks (with the downside of more costly inference), and could be used to produce large samples of synthetic observations tailored to a specific imaging survey. We demonstrate two potential uses of the DDPM: (1) accurate in-painting of occluded data, such as satellite trails, and (2) domain transfer, where new input images can be processed to mimic the properties of the DDPM training set. Here we ‘DESI-fy’ cartoon images as a proof of concept for domain transfer. Finally, we suggest potential applications for score-based approaches that could motivate further research on this topic within the astronomical community.

**Key words:** methods: data analysis – methods: statistical

## 1 INTRODUCTION

Synthetic data will play a pivotal role as we journey further into astronomy’s epoch of big data, especially for large extragalactic surveys (York et al. 2000; Dewdney et al. 2009; Amiaux et al. 2012; Ivezić et al. 2019). It will be required to train machine learning methods, to interpret observations, and to test theoretical frameworks. Indeed, one form of synthetic data comes from theoretical models. For example, in the field of galaxy formation and evolution, simulations using semi-analytical approaches have been successful in reproducing many of the bulk observable and emergent properties of galaxies over a significant fraction of cosmic time (e.g. Somerville & Primack 1999; Cole et al. 2000; Bower et al. 2006; Croton et al. 2006). Semi-analytical models (SAMs) employ approximations derived from more detailed numerical simulations and empirical calibrations from data to model galaxy formation and evolution. So it is possible to generate, for example, a ‘mock’ catalogue of galaxies with predicted optical photometry (Lagos et al. 2019). Hydrodynamical models of galaxy formation track the evolution of baryons and dark matter within representative volumes (e.g. Dubois et al. 2014; Vogelsberger et al. 2014; Schaye et al. 2015; Khandai et al. 2015;

Kaviraj et al. 2017), and when pushed to high spatial resolution, can predict galaxy morphologies on physical scales commensurate with the angular scales achievable with current observational facilities. When radiative transfer schemes are applied for the propagation of (for example) starlight through the volume, realistic synthetic observations can be produced, to be compared with nature (e.g. Camps et al. 2016; Trayford et al. 2017; Lovell et al. 2021).

To properly mimic real astronomical data, with all its wonderful idiosyncrasies, requires a full and detailed understanding of the telescope response, instrumental properties, and observing conditions, not to mention the nuances of any data reduction procedure. These non-trivial steps are typically unique to a given set of observations. There is a short-cut however: armed with enough examples of observations from a given survey, it should be possible to derive a data-driven approach to mimic not only the content of interest – astronomical signal – but also the properties of the data themselves. Deep generative models enable precisely that.

Great attention has been given to applications of deep generative learning to problems in astronomy lately. Generative Adversarial Networks (GAN; Goodfellow et al. 2014) have been used for deconvolution (Schawinski et al. 2017), synthetic galaxy generation (Ravanbakhsh et al. 2016; Fussell & Moews 2019), dark matter simulation (Mustafa et al. 2019; Tamosiunas et al. 2020), and deep

\* mike@mjjsmith.com

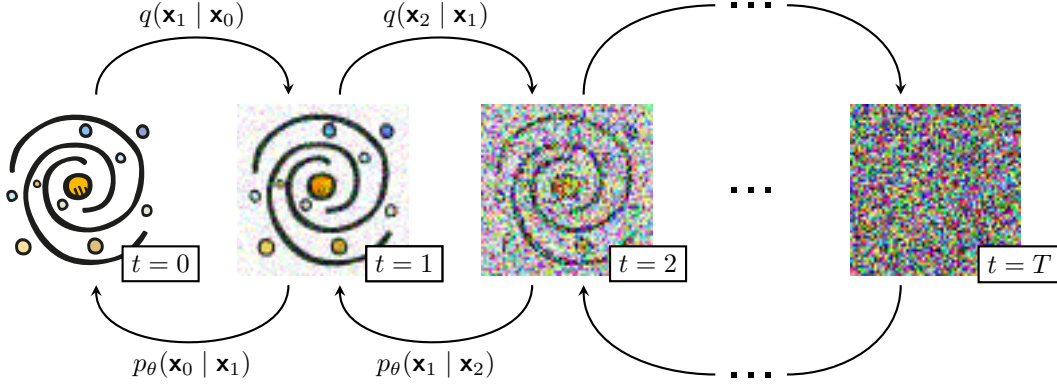


**Figure 1.** It is easy (and achievable without learnt parameters) to add noise to an image, but more difficult to remove it. DDPMs attempt to learn an iterative removal process through an appropriate neural network.  $p_\theta$ .

field imagery generation (Smith & Geach 2019). Variational Auto-Encoders (VAE; Kingma & Welling 2014) have been used to simulate galaxy observations (Ravanbakhsh et al. 2016; Spindler et al. 2021; Lanusse et al. 2021), as have flow-based models (Rezende & Mohamed 2015; Bretonnière et al. 2021). In this paper, we show that it is possible to simulate realistic galaxy imagery with a Denoising Diffusion Probabilistic Model (DDPM).

DDPMs were introduced by Sohl-Dickstein et al. (2015) and were first shown to produce high quality synthetic samples by Ho et al. (2020). They belong to a family of generative deep learning models that employ denoising ‘score matching’ via annealed Langevin dynamic sampling (Song & Ermon 2020; Ho et al. 2020; Jolicœur-Martineau et al. 2020; Song et al. 2021). This family of score-based generative models (SBGMs) can generate imagery of a quality and diversity surpassing state of the art GAN models, a startling result considering the historic disparity in interest and development between the two techniques (Song et al. 2021; Nichol & Dhariwal 2021; Dhariwal & Nichol 2021).

SBGMs have already been used to super-resolve images (Kadkhodaie & Simoncelli 2020; Saharia et al. 2021), translate between image domains (Sasaki et al. 2021), separate superimposed images (Jayaram & Thickstun 2020), and in-paint information (Kadkhodaie & Simoncelli 2020; Song et al. 2021). At the time of writing, there is only one example of score-based modelling in the astronomy literature (Remy et al. 2020). This is despite some obvious uses in astronomical data pipelines. For example: an implementation like Sasaki et al. (2021) could be used for survey-to-survey photometry translation similarly to Buncher et al. (2021); the source image separation model described in Jayaram & Thickstun (2020) could be applied as an astronomical object deblender (for example: Stark et al. 2018; Reiman & Göhre 2019; Arcelin et al. 2021); and information inpainting could be used to remove nuisance objects from observations (Kadkhodaie & Simoncelli 2020; Song et al. 2021).

This paper is organised as follows. Section 2 introduces the DDPM formulation used in this paper. In Section 3 and Section 4, we show that DDPMs are capable of generating diverse synthetic galaxy observations that are both statistically and qualitatively indistinguishable from observations found in the training set. We also demonstrate that DDPMs can in-paint occluded information in an observation, such as satellite trails<sup>1</sup>, and show that we can inject realism into entirely un-

realistic cartoon imagery. A discussion of our results and suggestions for future research are presented in Section 5.

## 2 DENOISING DIFFUSION PROBABILISTIC MODELS

Denoising Diffusion Probabilistic Models (DDPMs) define a diffusion process that projects a complex image domain space onto a simple domain space. In the original formulation, this diffusion process is fixed to a predefined Markov chain that adds a small amount of Gaussian noise with each step. Figure 1 illustrates that this ‘simple domain space’ can be noise sampled from a Gaussian distribution:  $\mathbf{x}_T \sim \mathcal{N}(\mathbf{0}, \mathbb{1})$ .

### 2.1 Forward process

We define a Markov chain to slowly add Gaussian noise to our data:

$$q(\mathbf{x}_{0\dots T}) = q(\mathbf{x}_0) \prod_{t=1}^T q(\mathbf{x}_t | \mathbf{x}_{t-1}). \quad (1)$$

The amount of noise added per step is controlled with a variance schedule  $\{\beta_t \in (0, 1)\}_{t=1}^T$ , such that

$$q(\mathbf{x}_t | \mathbf{x}_{t-1}) = \mathcal{N}(\mathbf{x}_t; \sqrt{1 - \beta_t} \mathbf{x}_{t-1}, \beta_t \mathbb{1}). \quad (2)$$

This process is applied iteratively to the input image,  $\mathbf{x}_0$ . If we define the above equation to only depend on  $\mathbf{x}_0$ , we can immediately calculate an image representation  $\mathbf{x}_t$  for any  $t$  (Ho et al. 2020). Defining  $\alpha_t = 1 - \beta_t$  and  $\bar{\alpha}_t = \prod_{i=1}^t \alpha_i$ :

$$\begin{aligned} \mathbf{x}_t &= \sqrt{\alpha_t} \mathbf{x}_{t-1} + \sqrt{1 - \alpha_t} \mathbf{z}_{t-1} \\ &= \sqrt{\alpha_t \alpha_{t-1}} \mathbf{x}_{t-2} + \sqrt{(1 - \alpha_t) + \alpha_t (1 - \alpha_{t-1})} \bar{\mathbf{z}}_{t-2} \\ &= \sqrt{\alpha_t \alpha_{t-1} \alpha_{t-2}} \mathbf{x}_{t-3} + \sqrt{(1 - \alpha_t \alpha_{t-1}) + \alpha_t \alpha_{t-1} (1 - \alpha_{t-2})} \bar{\mathbf{z}}_{t-3} \\ &= \dots \\ &= \sqrt{\bar{\alpha}_t} \mathbf{x}_0 + \sqrt{1 - \bar{\alpha}_t} \mathbf{z}, \end{aligned} \quad (3)$$

where  $\mathbf{z} \sim \mathcal{N}(\mathbf{0}, \mathbb{1})$  and  $\bar{\mathbf{z}}$  is a combination of Gaussians. Substituting this expression into Equation 2 removes the  $\mathbf{x}_{t-1}$  dependency and yields

$$q(\mathbf{x}_t | \mathbf{x}_0) = \mathcal{N}(\mathbf{x}_t; \sqrt{\bar{\alpha}_t} \mathbf{x}_0, (1 - \bar{\alpha}_t) \mathbb{1}). \quad (4)$$

<sup>1</sup> A growing problem due to the rapidly increasing population of satellites, exacerbated by mega-constellations (Kocifaj et al. 2021).

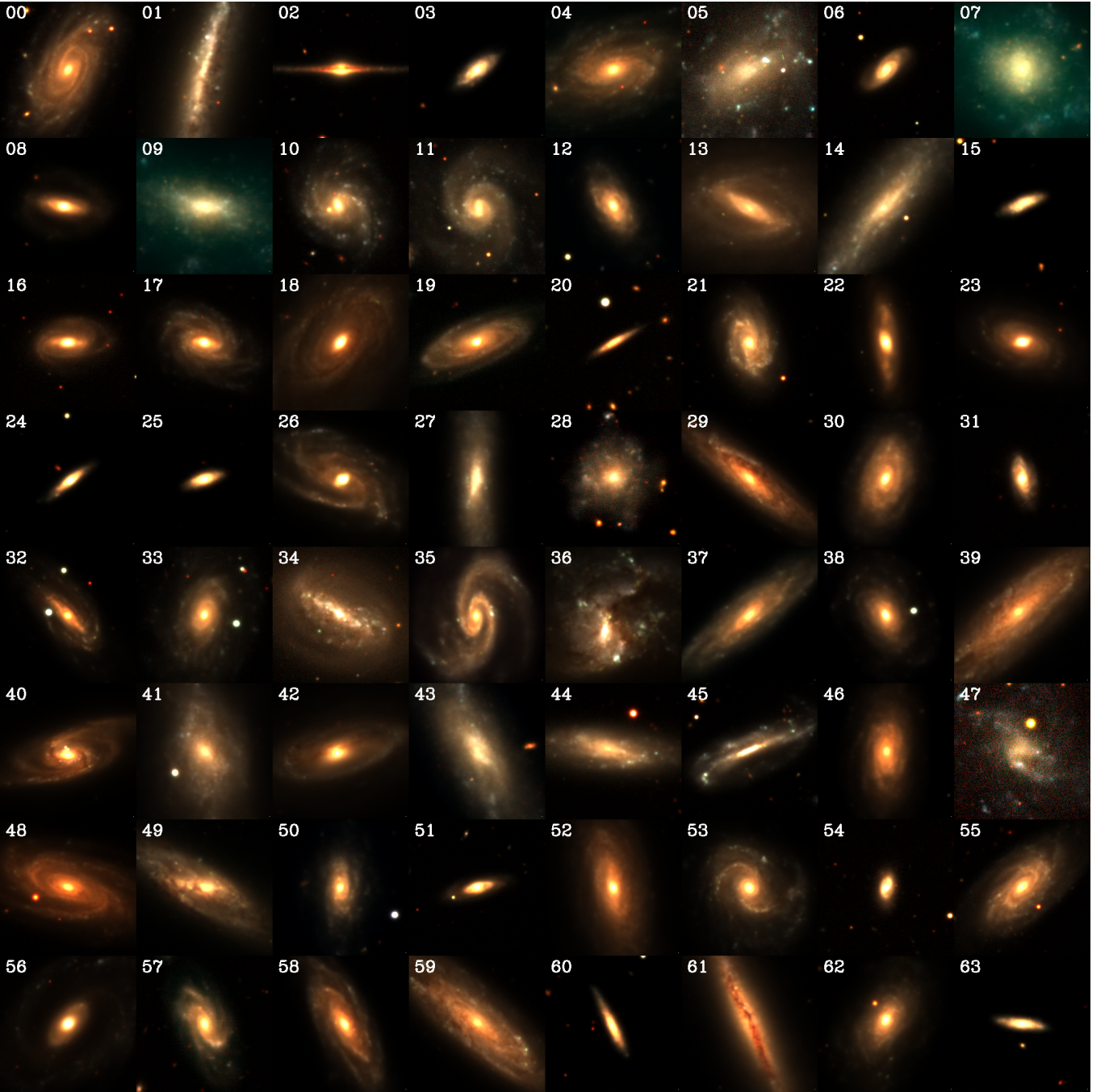


**Figure 2.** A montage of generated galaxies designed to mimic the PROBES data set, interspersed with real examples from the dataset itself. The images have been shuffled and the synthetic/real data split is 50/50. All images are *grz* RGB composites with identical scaling (we have performed a 99.5% percentile clip to better show low surface brightness features). A key stating which galaxies are real and which are generated is provided at the end of this manuscript. More generated galaxies can be found at <http://mjjsmith.com/thisisnotagalaxy>.

## 2.2 Reverse process

DDPMs attempt to reverse the forward process by applying a Markov chain with learnt Gaussian transitions. In our case these transitions are learnt via an appropriate neural network,  $p_\theta$ :

$$p_\theta(\mathbf{x}_0 \dots \mathbf{x}_T) = p(\mathbf{x}_T) \prod_{t=1}^T p_\theta(\mathbf{x}_{t-1} | \mathbf{x}_t), \quad (5)$$

$$p_\theta(\mathbf{x}_{t-1} | \mathbf{x}_t) = \mathcal{N}(\mathbf{x}_{t-1}; \boldsymbol{\mu}_\theta(\mathbf{x}_t, t), \boldsymbol{\Sigma}_\theta(\mathbf{x}_t, t)). \quad (6)$$

While  $\boldsymbol{\Sigma}_\theta(\mathbf{x}_t, t)$  can be learnt<sup>2</sup>, we follow Ho et al. (2020) and fix it to an iteration-dependent constant  $\sigma_t^2 \mathbb{1}$ , where  $\sigma_t^2 = 1 - \alpha_t$ .

By recognising that DDPMs are a restricted class of Hierarchical VAE, we see that we can train  $p_\theta$  by optimising the evidence lower bound (ELBO, introduced in Kingma & Welling 2014) that can be written as a summation over the Kullback-Leibler divergences at each

<sup>2</sup> See for example Nichol & Dhariwal (2021).

iteration step<sup>3</sup>:

$$\begin{aligned} \mathcal{L}_{\text{ELBO}} = \mathbb{E}_q \left[ D_{\text{KL}}(q(\mathbf{x}_T | \mathbf{x}_0) \| p(\mathbf{x}_T)) \right. \\ \left. + \sum_{t>1} D_{\text{KL}}(q(\mathbf{x}_{t-1} | \mathbf{x}_t, \mathbf{x}_0) \| p_{\theta}(\mathbf{x}_{t-1} | \mathbf{x}_t)) \right. \\ \left. + \log p_{\theta}(\mathbf{x}_0 | \mathbf{x}_1) \right]. \end{aligned} \quad (7)$$

In the Ho et al. (2020) formulation, the first term in Equation 7 is a constant during training and the final term is modelled as an independent discrete decoder. This leaves the middle summation. Each term in that summation can be written as

$$\mathcal{L}(\boldsymbol{\mu}_t, \boldsymbol{\mu}_{\theta}) = \frac{1}{2\sigma_t^2} \|\boldsymbol{\mu}_t(\mathbf{x}_t, \mathbf{x}_0) - \boldsymbol{\mu}_{\theta}(\mathbf{x}_t, t)\|^2, \quad (8)$$

where  $\boldsymbol{\mu}_{\theta}$  is the neural network’s estimation of the forward process posterior mean  $\boldsymbol{\mu}_t$ . In practice it would be preferable to predict the noise addition in each iteration step ( $\mathbf{z}_t$ ), as  $\mathbf{z}_t$  has a distribution that by definition is centred about 0, with a well defined variance. To this end we can define  $\boldsymbol{\mu}_{\theta}$  as

$$\boldsymbol{\mu}_{\theta}(\mathbf{x}_t, t) = \frac{1}{\sqrt{\alpha_t}} \left( \mathbf{x}_t - \frac{1 - \alpha_t}{\sqrt{1 - \bar{\alpha}_t}} \mathbf{z}_{\theta}(\mathbf{x}_t, t) \right), \quad (9)$$

and by combining Equations 8 and 9 we get

$$\begin{aligned} \mathcal{L}(\mathbf{z}_t, \mathbf{z}_{\theta}) = \frac{1}{2\sigma_t^2} \left\| \frac{1}{\sqrt{\alpha_t}} \left( \mathbf{x}_t - \frac{1 - \alpha_t}{\sqrt{1 - \bar{\alpha}_t}} \mathbf{z}_t \right) - \right. \\ \left. \frac{1}{\sqrt{\alpha_t}} \left( \mathbf{x}_t - \frac{1 - \alpha_t}{\sqrt{1 - \bar{\alpha}_t}} \mathbf{z}_{\theta}(\mathbf{x}_t, t) \right) \right\|^2 \\ = \frac{(1 - \alpha_t)^2}{2\sigma_t^2 \alpha_t (1 - \bar{\alpha}_t)} \|\mathbf{z}_t - \mathbf{z}_{\theta}(\mathbf{x}_t, t)\|^2. \end{aligned} \quad (10)$$

Ho et al. (2020) empirically found that a simplified version of the loss described in Equation 10 results in better sample quality. We therefore use a simplified version of Equation 10 as our loss, and optimise to predict the noise required to reverse a forward process iteration step:

$$\mathcal{L}(\mathbf{z}_t, \mathbf{z}_{\theta}) = \|\mathbf{z}_t - \mathbf{z}_{\theta}(\mathbf{x}_t, t)\|^2, \quad (11)$$

where  $\mathbf{x}_t = \sqrt{\alpha_t} \mathbf{x}_0 + \sqrt{1 - \alpha_t} \mathbf{z}_t$ .

By recognising that  $\mathbf{z}_t = \sigma_t^{-2} \nabla_{\mathbf{x}_t} \log q(\mathbf{x}_t | \mathbf{x}_{t-1})$ , we see that Equation 11 is equivalent to denoising score matching over  $t$  noise levels (Vincent 2011). This connection establishes a link between DDPMs and other SBGMs (such as Song & Ermon 2019, 2020; Jolicœur-Martineau et al. 2020).

Here we use a modified U-Net as  $p_{\theta}$  (Ronneberger et al. 2015; Salimans et al. 2017), and train via the Adam optimiser (Kingma & Ba 2015). The U-Net comprises of three downsample blocks, a bottleneck block, and three upsample blocks. Each downsample block comprises of two residual blocks (Srivastava et al. 2015; He et al. 2015), a self-attention layer (Bahdanau et al. 2014; Cheng et al. 2016), and a strided convolution layer. The bottleneck comprises of a self-attention layer sandwiched by two residual blocks. Each upsample block comprises of two residual blocks, a self-attention layer, and a transposed convolution layer. As in a standard U-Net, residual connections link the downsample and upsample blocks. To provide information about the current iteration step, an embedding representing the reverse process iteration step is periodically injected into the

<sup>3</sup> See Appendix B in Sohl-Dickstein et al. (2015) and Appendix A in Ho et al. (2020) for the full derivation.

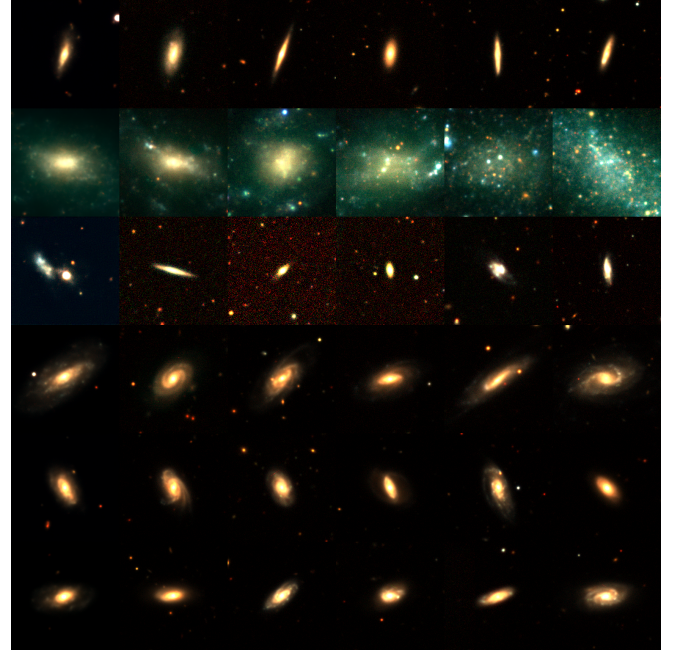


**Figure 3.** Pixelspace nearest neighbour to generated PROBES galaxies. The leftmost column shows a galaxy generated with the model  $p_{\theta}(\mathbf{z})$ , the other columns show that galaxy’s closest training set neighbours in pixelspace. Moving along a row takes us further away from the simulated galaxy in pixelspace.

U-Net via a summation. Mish activation is used throughout (Misra 2019). The full implementation is released under the AGPLv3 licence and is available at <https://github.com/Smith42/astroddpm>.

To run inference for the reverse process, we progressively remove the predicted noise  $\mathbf{z}_{\theta}$  from our image. The predicted noise is weighted according to our variance schedule:

$$\mathbf{x}_{t-1} = \frac{1}{\sqrt{\alpha_t}} \left( \mathbf{x}_t - \frac{1 - \alpha_t}{\sqrt{1 - \bar{\alpha}_t}} \mathbf{z}_{\theta}(\mathbf{x}_t, t) \right) + \sigma_t \mathbf{z}. \quad (12)$$

If we take  $p(\mathbf{x}_T) \sim \mathcal{N}(\mathbf{x}_T; \mathbf{0}, \mathbf{1})$ , we can use  $p_{\theta}$  to generate entirely novel data that are similar, but not identical to, those found in the training set. We can also use  $p_{\theta}$  to perform image domain translation, and inpainting. Section 4 describes these applications in further detail.

### 3 SIMULATING DESI GALAXY IMAGES

We train our models on minimally processed native resolution ( $256 \times 256$  pixels at  $0.262'' \text{ pixel}^{-1}$ ) Dark Energy Spectroscopic Instrument (DESI; Dey et al. 2019) Legacy Survey Data Release 9 galaxy imagery. The  $g$ ,  $r$ , and  $z$  band images have an average atmospheric seeing of approximately  $1''$ .

#### 3.1 Data sample, preparation, and training

We train two models on two different datasets for 750,000 global steps each across three NVIDIA Tesla V100 GPUs, corresponding to  $\sim 250$  hours wall time per model. We fill all available VRAM and set the batch size to 56. The two datasets are described below.

(i) We train on the Photometry and Rotation curve OBServations from Extragalactic Surveys (PROBES) galaxy dataset as imaged by

the Dark Energy Spectroscopic Instrument (DESI; Dey et al. 2019) Legacy Survey Data Release 9. The PROBES dataset is described in Stone & Courteau (2019) and Stone et al. (2021). It contains 1962 late-type galaxies with no large neighbours or other obscuring features (such as bright stars). Most of the objects are well resolved, exhibiting spiral arms, bars, and other features characteristic of late-type systems. The model trained on this dataset produces galaxies that obviously exhibit internal structure. We refer to this as the ‘PROBES’ dataset.

(ii) We also train on a dataset of 306 006 galaxies whose coordinates are taken from Sloan Digital Sky Survey (SDSS; York et al. 2000) Data Release 7 (Abazajian et al. 2009) and a modified catalogue from Wilman et al. (2010). This volume complete sample has an  $r$ -band absolute magnitude limit of  $M_r \leq -20$  and a redshift limit of  $z \leq 0.08$ . See Arora et al. (2019) for details. This catalogue covers a wide range of environments from clusters to groups and field systems. As in the PROBES dataset, the galaxy images are taken from DESI (Dey et al. 2019). We use this dataset and the corresponding trained model to compare population level galaxy statistics (Sec. 4.1). For brevity we refer to this as the ‘SDSS’ dataset.

All images are cropped about the target galaxy to a shape of  $256 \times 256$  pixels. The only destructive pre-processing performed is an upper and lower percentile clipping, with the percentiles calculated across the entire dataset. This clipping removes any ‘hot’ or ‘cold’ pixels. To calculate the upper flux truncation point we evaluate the 99.9th percentile fluxes for each galaxy across the full dataset. To separate the long tail from the bulk of the data, we fit a two-cluster  $k$ -means (Lloyd 1982). The two-cluster  $k$ -means returns a boundary at approximately 5 analogue-to-digital unit (ADU) for the SDSS dataset, and 5.5 ADU for the PROBES dataset, and so we set these values as our upper truncation points and normalisation constants. The lower flux truncation point is set as the minimum off-source pixel-wise root mean square across the entire dataset. We found this value to be very close to zero across all bands in both the SDSS and PROBES datasets, and therefore set the lower flux truncation as 0 ADU. We apply a min-max normalisation to the images with the following equation:

$$\bar{x} = \frac{2 \cdot \max(0, \min(x, A))}{A} - 1, \quad (13)$$

with  $A = 5.0$  ADU being the upper flux truncation for the SDSS dataset, and  $A = 5.5$  ADU for the PROBES dataset. We reverse this normalisation when post-processing inferences from the model.

## 4 RESULTS

Figure 2 shows a random selection of generated galaxies, alongside a random selection of real galaxies. The images are shuffled and we can see that the simulated and real galaxies are subjectively indistinguishable, at least to the authors (we of course invite the reader to make their own assessment of fidelity, referring to the answer key given at the end of this paper). Figure 3 presents a random selection of generated galaxies’ nearest neighbours in pixelspace. Since the pixelspace search does not return identical galaxies, we conclude that the DDPM is not simply regurgitating imagery, and is indeed generating novel data. We found a systematic offset in the simulated pixel fluxes and corrected for it in post-processing. To estimate the offset, we calculated the median pixel value in each of the 10,000 mock and 10,000 real galaxy observations. Each set is sorted and the medians paired according to their place in the sorted sets. Finally we fit a linear function to the resulting 10,000 median flux pairs.

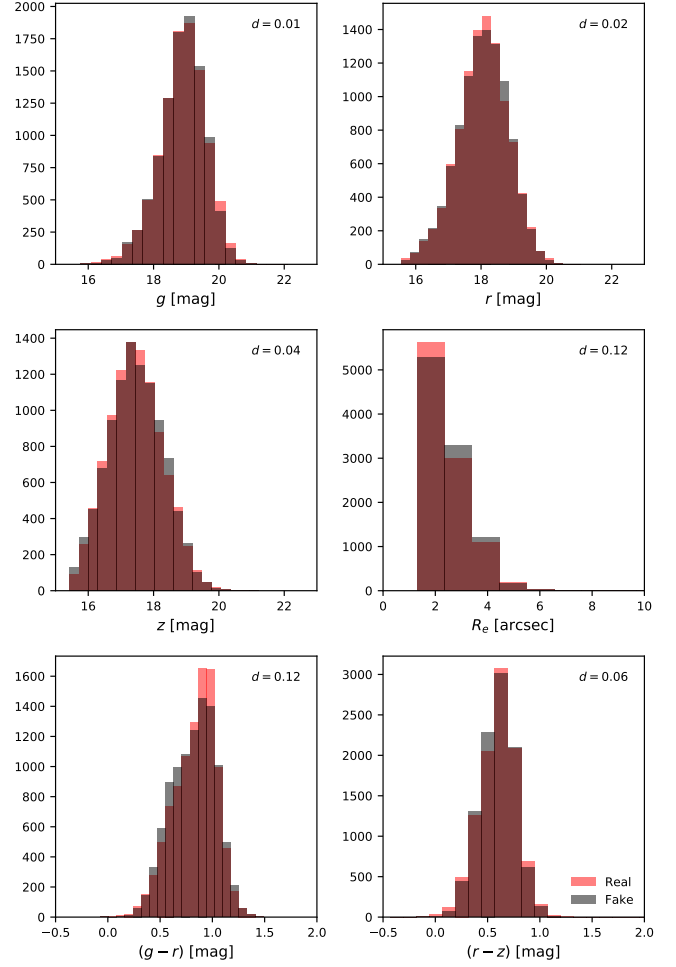


**Figure 4.** Histogram comparison between galaxies generated by the SDSS DDPM, and galaxies contained in the SDSS training set. The half light radius histogram follows a lognormal distribution, as do the magnitude and colour histograms in flux space. Therefore, we can calculate Cohen’s  $d$  effect size for each histogram pair. As a rule of thumb, if  $d \leq 0.2$  the effect size is considered ‘small’ and a sign of negligible difference (Cohen 1988).

The gradient of the fit was used as a scaling factor for the simulated galaxy images. We found the multiplier to be 1.18 in  $g$ , 1.16 in  $r$ , and 1.23 in  $z$  for our DESI observations. Unfortunately, the exact cause of these offsets could not be determined. We propose that this discrepancy is due to a fundamental property of the neural network and its interaction with sparse imagery such as our galaxy images.

### 4.1 Quantifying similarity

To quantify the similarity of the visual and morphological characteristics of our galaxies, we borrow from the deep generative learning literature and calculate the Fréchet Inception Distance (FID; Heusel et al. 2017; Seitzer 2020). The FID is the distance (Dowson & Landau 1982) between Gaussians fitted to two Inception-v3 (Szegedy et al. 2016) penultimate layer feature representations. The penultimate layer nodes are deep in the network and mimic a human’s perception when viewing images. Therefore, if the Gaussians are similar (and the corresponding FID is small), the images will be visually similar too.

We run FID on 10,000 random samples and present the results in Table 1. While we cannot yet contextualise our FID within the

**Table 1.** Wasserstein-1 distance between emergent property distributions.  $p_\theta(\mathbf{z})$  is the DDPM described in this paper. ‘SDSS’ is a comparison between two different randomly selected sets of 10,000 galaxies from the training set. We provide the ‘SDSS’ Wasserstein-1 distances as a baseline ‘perfect’ inference.

	$W_g$	$W_r$	$W_z$	$W_{R_e}$	$W_{(g-r)}$	$W_{(r-z)}$	SGD	FID
$p_\theta(\mathbf{z})$	0.013	0.012	0.023	0.055	0.015	0.010	0.127	19
SDSS	0.008	0.010	0.014	0.018	0.006	0.004	0.060	0.95

literature, we provide the value for future comparison. Figure 2 is presented for a basic visual and morphological comparison; we cannot discern between the synthesised and real galaxies, which suggests that the visual and morphological characteristics of our datasets are well replicated.

To demonstrate that we capture emergent, measurable properties of the galaxies, we directly compare size and flux distributions. Fluxes are measured via a summation within a fixed aperture with a diameter of 12 pixels ( $\sim 3''$ ), and we use the half light radius as a simple measure of size. To summarise the distance between the ‘ground truth’ photometry training set properties and the properties of the simulated set we use the Wasserstein-1 distance<sup>4</sup>:

$$W(u, v) = \int_{-\infty}^{\infty} |U - V| \quad (14)$$

where  $U$  and  $V$  are the respective cumulative distribution functions of  $u$  and  $v$ .

Following Equation 14, we propose a ‘synthetic galaxy distance’ metric that captures the difference between emergent properties of a synthetic and reference galaxy photometry dataset:

$$\begin{aligned} \text{SGD} &= \sum_i W(u_i, v_i), \\ &= W(R_e^u, R_e^v) + W(g^u, g^v) + W(r^u, r^v) + W(z^u, z^v) + \\ &\quad W((g-r)^u, (g-r)^v) + W((r-z)^u, (r-z)^v), \end{aligned} \quad (15)$$

where  $R_e$  is the half light radius, and  $g$ ,  $r$ , and  $z$  are aperture magnitudes in specific bands and  $u$  and  $v$  denote different datasets. The SGD returns a single number, where a lower value denotes a closer match between  $u$  and  $v$ . When combined with the FID for visual and morphological similarity, a good overview of the similarity between two large galaxy photometry datasets is obtained. Figure 4 shows the results for the individual tests and the SGD summary is in Table 1. We run SGD on 10,000 random samples.

While we cannot yet contextualise our SGD within the literature, we provide the value for future comparison. We also present Figure 4 to otherwise show that our model captures physical properties of the galaxies. We calculate Cohen’s  $d$  effect size for each histogram pair, and in all cases find  $d \leq 0.2$  indicating a ‘small’ or negligible effect (Cohen 1988). Cohen’s  $d$  effect size is defined here as

$$d = \left| \sqrt{\frac{2}{\sigma_u^2 + \sigma_v^2}} (\mu_u - \mu_v) \right|, \quad (16)$$

where  $\mu$  is the mean of the fitted distribution, and  $\sigma$  is the standard deviation. The subscripts  $u$  and  $v$  denote different datasets.

<sup>4</sup> Since we are dealing with large datasets a Kolmogorov-Smirnov (KS) test is not appropriate as it becomes overpowered with a very large sample size. We instead use the related Wasserstein-1 distance to provide an absolute value that represents the difference between our distribution pairs, and also calculate Cohen’s  $d$  effect size as a direct intuitive substitution for the  $p$ -values that would otherwise result from KS tests (Figure 4).

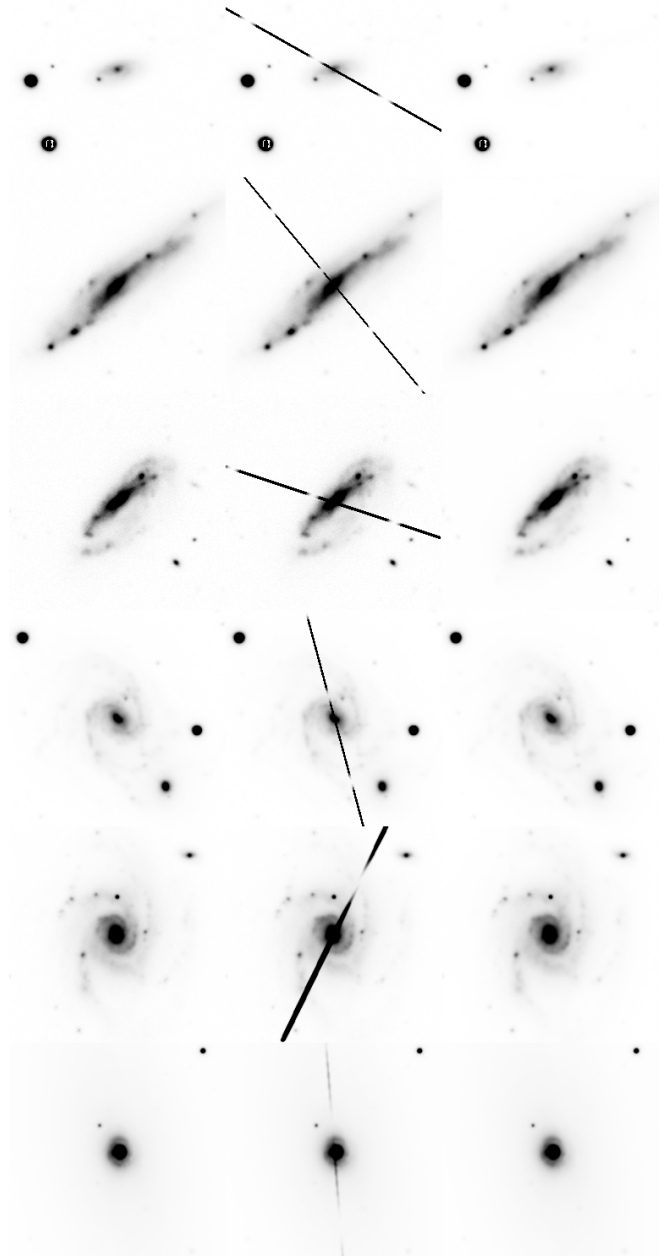


**Figure 5.** Inpainting of galaxy observations defaced by satellite trails. The first column shows the original ( $r$ -band) PROBES galaxy,  $\mathbf{x}$ . The second column shows the defaced galaxy,  $\tilde{\mathbf{x}}$ . The third column shows a random guided draw from the model  $p_\theta(q(\tilde{\mathbf{x}}; T = 950))$ .

## 4.2 Satellite trail removal via guided diffusion

The DDPM can be used to remove simulated galaxy satellite trails from images. We simulate satellite trails by superimposing a bright linear strip onto a real image. The strips have a random direction, brightness, width, and periodicity. In this demonstration we present monochrome  $r$ -band images from the PROBES dataset.

To perform guided diffusion, we run the reverse process on the occluded part of the galaxy, in this case the satellite trails. The other image pixels are drawn directly from the forward process, and so are not updated. The occluded pixels are updated with guidance information from the surrounding pixels. As Figures 5 and 6 show, this

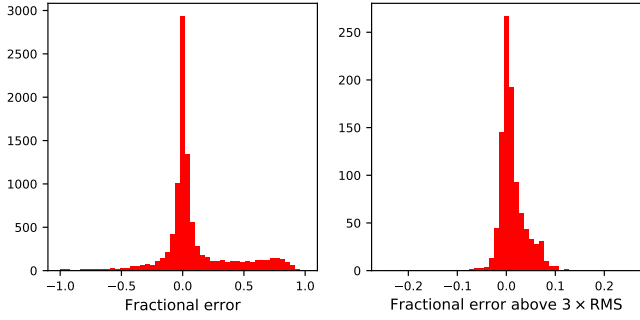


**Figure 6.** A pixelwise comparison between the ground truth images’ occluded fluxes, and the recovered images’ in Figure 5, expressed as a fractional error. The left panel shows the residual for all pixels, and the right panel restricts the analysis to pixels exceeding 3 times the background r.m.s. (0.654 ADU). We find good agreement between the predicted pixel fluxes and the ground truth fluxes, with virtually all significant pixels within 10% of their true values.

process retrieves excellent representations of the original galaxies, essentially in-painting the missing data with high accuracy. Figure 6 shows that significant ( $>3\sigma$ ) pixels that were occluded by a trail have recovered fluxes within 10% of their true values. Since satellite trails are not present in the training set, a guided draw from the learnt model is effective at ‘interpolating’ the occluded pixels. A similar approach would work for other unwanted artefacts, such as glints and ghosts, provided they do not appear frequently in the training set.

### 4.3 Domain transfer

The DDPM can also be used to make another input image resemble a DESI Legacy Survey observation. To perform this domain transfer, we first run the forward process for  $T$  iterations. We then take the noisy image, and run the reverse process. This results in a DESI Legacy Survey-like observation that shares high level features with the input image. Figure 7 demonstrates this technique on cartoons, setting  $T = 600$ . If  $T$  is set at a high value, the DDPM produces an image that more closely resembles one that might be found in the training set. However, fine detail in the conditioning image is lost as it is erased by the forward noise addition process. The cartoon input is transformed into an image resembling it, but with the properties of a DESI survey image. Once the cartoon images have been ‘DESI-fied’, we can search for the nearest neighbour in pixelspace in the real dataset, and this is shown as a final column in Figure 7. Thus, this approach paves the way for pixel-based searching of large survey imaging databases. For example, one could potentially sketch a particular morphology or configuration (e.g. an Einstein ring), apply the model tailored to that survey and then recover the best match in the real data. One could also apply this technique to inject realism into simulated galaxies, such as those predicted by hydrodynamical simulations.

Since the first release of this paper Preechakul et al. (2021) and Saharia et al. (2021) have both explored image-to-image translation with a score-based model. Preechakul et al. (2021) showed that DDPMs can produce semantically meaningful embeddings, given an appropriate architecture. In their paper, they demonstrate that their autoencoding DDPM can interpolate along the embedding space and age and de-age images of faces. In astronomy, one can imagine using a ‘survey’ embedding to interpolate between surveys.

Saharia et al. (2021) took a different approach and explicitly trained their model to reverse the forward process of an ill-posed inverse problem. For an ill-posed inverse problem such as noise addition, one can define the forward process in a classical way, and use a

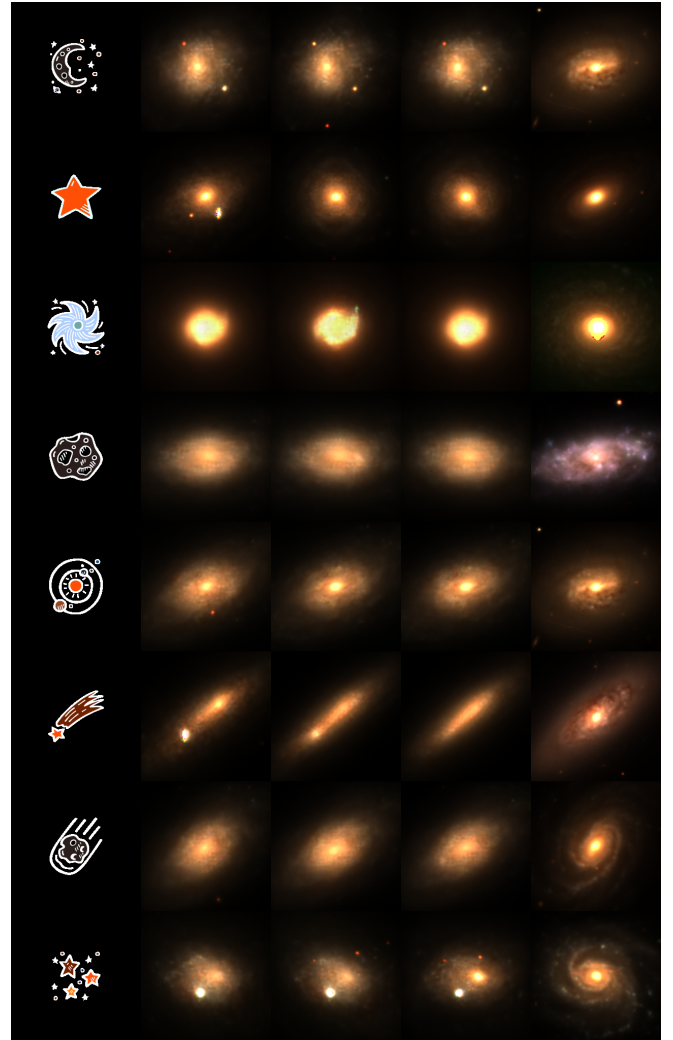


**Figure 7.** Cartoon images are made to look like DESI observations via the model  $p_{\theta}(q(x;T = 600))$ . The first column shows the input image, the middle columns show random draws from the PROBES model, and the final column shows the pixelspace nearest neighbour to the generated images.

DDPM in the inverse process to retrieve the uncorrupted image. Saharia et al. (2021) did this and showed that a DDPM can colourise greyscale images, and remove JPEG compression artefacts.

For more difficult problems that do not have a well defined forward process, we can use a model similar to that introduced in Sasaki et al. (2021) to translate between two different image domains. We intend to explore astronomy related image-to-image translation applications more deeply in follow up work.

### 4.4 A fun aside: mock Astronomy Picture of the Day

As a fun aside, we have trained a DDPM on images from NASA’s Astronomy Picture of the Day (APOD) archive. The dataset comprises 11,428 RGB JPEG images resized to a  $256 \times 256$  shape. We trained this model for 900,000 global steps on a single V100 GPU. This allows us to generate new APODs that do not actually exist. Figure 8 shows a curated sample of ‘AI-APODs’ generated from this model. We leave it to the reader to critically assess their merits, but some common themes are apparent: images resembling nebulae, galaxies, landscapes, moons, and aurorae are

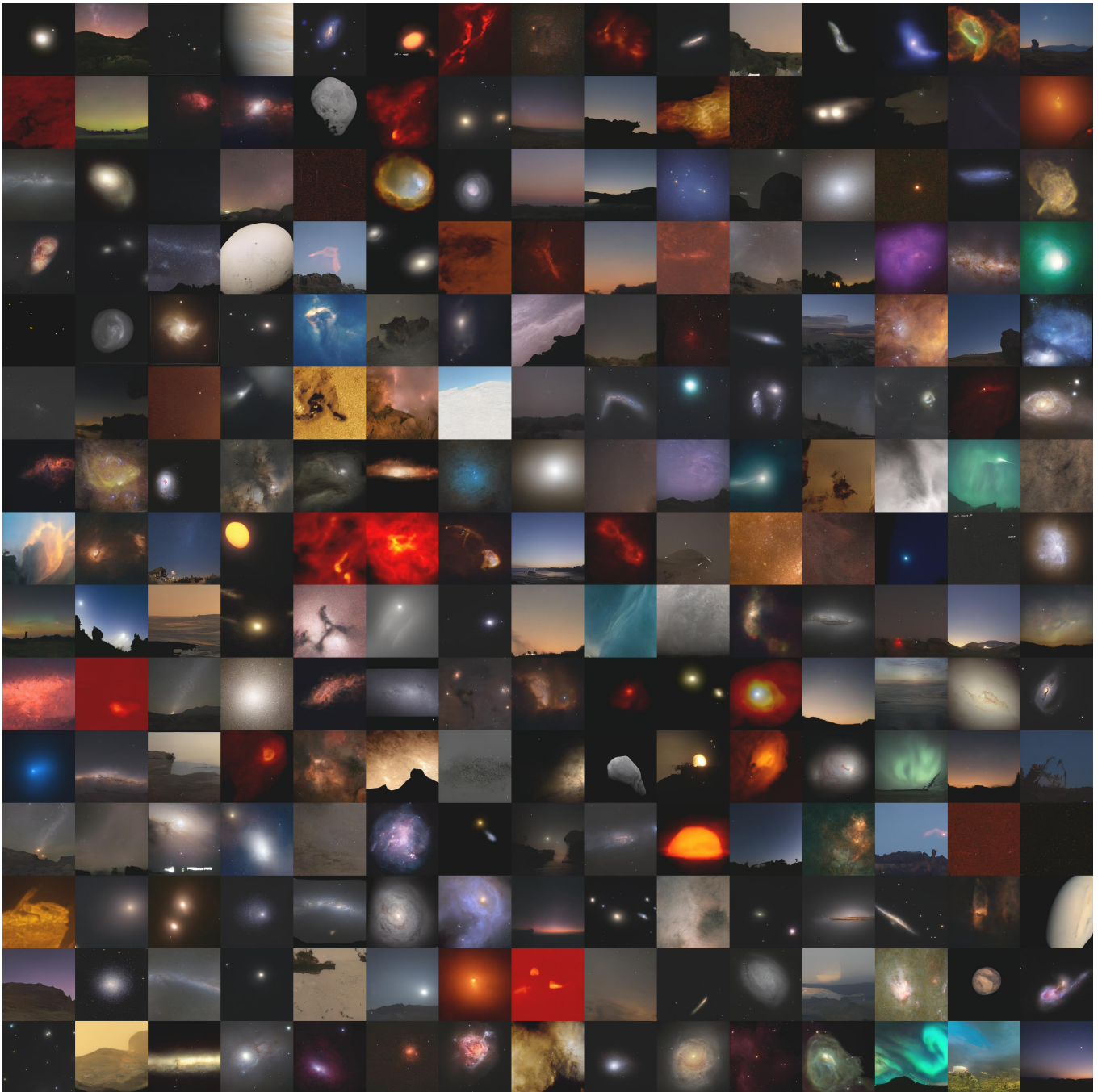


**Figure 8.** A sample of DDPM-generated APOD imagery: AI-APODs. More can be found at <http://mjjsmith.com/thisisnotanapod> and you can follow a Twitter bot <https://twitter.com/ThisIsNotAnApod>. A version of this figure has been featured on NASA's APOD <https://apod.nasa.gov/apod/ap211109.html>.

present. Random AI-APODs generated from the model can be found at <http://mjjsmith.com/thisisnotanapod>, and a Twitter bot will post images at <https://twitter.com/ThisIsNotAnApod>.

## 5 CONCLUSIONS

We show that score-based generative modelling is a viable method for synthetic galaxy image generation, and that this approach preserves emergent properties such as galaxy size and total flux over different photometric bands, in addition to producing realistic morpholo-

gies. We achieve this fidelity without explicit encoding of physics or instrumental effects, a great advantage when simulating physically ill-defined objects. This is a completely data-driven approach to synthetic data generation.

There are downsides. Naturally, SBGMs require significant computational resources to train. However, unlike most other generative deep learning methods SBGMs also require significant resources to infer data. Since they need to diffuse the data for  $T$  cycles<sup>5</sup>, it takes

<sup>5</sup> In this work,  $T = 1000$



$T$  times longer to produce a batch of synthetic data compared to an equivalent GAN, VAE, or other single shot generative model. However, there may be routes to reduce the inference time for SBGMs, with promising results already (Jolicœur-Martineau et al. 2021; Song et al. 2021).

SBGMs have clear astronomical applications, from object deblending (Jayaram & Thickstun 2020) to survey-to-survey translation (Sasaki et al. 2021) to occluded object in-painting (Kadkhodaie & Simoncelli 2020; Song et al. 2021) to super-resolving imagery (Saharia et al. 2021). Unlike GANs, SBGMs do not suffer from mode collapse and are trivial to train. SBGMs produce imagery that has a diversity and fidelity that rivals state of the art GAN models (Song et al. 2021; Nichol & Dhariwal 2021; Dhariwal & Nichol 2021). Unlike VAEs, SBGMs do not constrain information to a fixed bottleneck vector and thus do not suffer from blurring, and instead produce sharp, realistic imagery (Spindler et al. 2021). For all these reasons, we believe that SBGMs are ripe for exploitation by the astronomical community, and we hope this paper motivates further work in this topic.

## DATA AND CODE AVAILABILITY

The full PyTorch (Paszke et al. 2019) implementation of the model presented here is available at <https://github.com/Smith42/astroddpm>, and the code to calculate the Synthetic Galaxy Distance (SGD) can be accessed at <https://github.com/Smith42/synthetic-galaxy-distance>. To calculate the Fréchet Inception Distance (FID), we used <https://github.com/mseitzer/pytorch-fid>.

## CARBON EMISSIONS

The training of deep learning models requires considerable energy, contributing to carbon emissions. The energy used to train AstroDDPM to completion is estimated to be 450 kWh, corresponding to 105 kg CO<sub>2</sub>e according to the Machine Learning Emissions Calculator described in Lacoste et al. (2019). To counteract further emission from redundant retraining, we follow the recommendations of Strubell et al. (2019) and make available the fully trained models, as well as the code to run them. Also, we will make available trained models for any improvements that we make to AstroDDPM in the future.

## ANSWER KEY FOR FIGURE 2

00 Real, 01 Real, 02 Real, 03 Mock, 04 Real, 05 Real, 06 Real, 07 Mock, 08 Mock, 09 Mock, 10 Real, 11 Real, 12 Mock, 13 Mock, 14 Mock, 15 Mock, 16 Real, 17 Real, 18 Mock, 19 Real, 20 Real, 21 Real, 22 Real, 23 Mock, 24 Mock, 25 Mock, 26 Mock, 27 Mock, 28 Mock, 29 Real, 30 Mock, 31 Real, 32 Real, 33 Real, 34 Real, 35 Mock, 36 Real, 37 Mock, 38 Mock, 39 Mock, 40 Mock, 41 Mock, 42 Mock, 43 Mock, 44 Real, 45 Real, 46 Mock, 47 Real, 48 Real, 49 Real, 50 Mock, 51 Real, 52 Mock, 53 Real, 54 Real, 55 Real, 56 Real, 57 Real, 58 Mock, 59 Real, 60 Mock, 61 Mock, 62 Mock, 63 Mock

## ACKNOWLEDGEMENTS

JEG is supported by the Royal Society. This research made use of the University of Hertfordshire’s High Performance Com-

puting facility (<http://uhhpc.herts.ac.uk/>). The galaxy icon in Figure 1, and the cartoons in Figure 7 are by Agata Kuczmińska and are available under the CC-BY-4.0 licence at <https://goodstuffnononsense.com/hand-drawn-icons/space-icons/>. We are grateful to the Natural Sciences and Engineering Research Council of Canada, the Ontario Government, and Queen’s University for critical support through various scholarships and grants. This work was supported in part by the Yonsei University Research Fund (Yonsei Frontier Lab. Young Researcher Supporting Program) of 2021. RAJ acknowledges support from the Korean National Research Foundation (NRF-2020R1A2C3003769). We thank the MNRAS reviewer for helpful comments and suggestions.

The Legacy Surveys consist of three individual and complementary projects: the Dark Energy Camera Legacy Survey (DECaLS; Proposal ID #2014B-0404; PIs: David Schlegel and Arjun Dey), the Beijing-Arizona Sky Survey (BASS; NOAO Prop. ID #2015A-0801; PIs: Zhou Xu and Xiaohui Fan), and the Mayall z-band Legacy Survey (MzLS; Prop. ID #2016A-0453; PI: Arjun Dey). DECaLS, BASS and MzLS together include data obtained, respectively, at the Blanco telescope, Cerro Tololo Inter-American Observatory, NSF’s NOIRLab; the Bok telescope, Steward Observatory, University of Arizona; and the Mayall telescope, Kitt Peak National Observatory, NOIRLab. The Legacy Surveys project is honoured to be permitted to conduct astronomical research on Iolkam Du’ag (Kitt Peak), a mountain with particular significance to the Tohono O’odham Nation.

NOIRLab is operated by the Association of Universities for Research in Astronomy (AURA) under a cooperative agreement with the National Science Foundation.

This project used data obtained with the Dark Energy Camera (DECam), which was constructed by the Dark Energy Survey (DES) collaboration. Funding for the DES Projects has been provided by the U.S. Department of Energy, the U.S. National Science Foundation, the Ministry of Science and Education of Spain, the Science and Technology Facilities Council of the United Kingdom, the Higher Education Funding Council for England, the National Center for Supercomputing Applications at the University of Illinois at Urbana-Champaign, the Kavli Institute of Cosmological Physics at the University of Chicago, Center for Cosmology and Astro-Particle Physics at the Ohio State University, the Mitchell Institute for Fundamental Physics and Astronomy at Texas A&M University, Financiadora de Estudos e Projetos, Fundacao Carlos Chagas Filho de Amparo, Financiadora de Estudos e Projetos, Fundacao Carlos Chagas Filho de Amparo, Conselho Nacional de Desenvolvimento Científico e Tecnológico and the Ministerio da Ciencia, Tecnologia e Inovacao, the Deutsche Forschungsgemeinschaft and the Collaborating Institutions in the Dark Energy Survey. The Collaborating Institutions are Argonne National Laboratory, the University of California at Santa Cruz, the University of Cambridge, Centro de Investigaciones Energeticas, Medioambientales y Tecnologicas-Madrid, the University of Chicago, University College London, the DES-Brazil Consortium, the University of Edinburgh, the Eidgenössische Technische Hochschule (ETH) Zurich, Fermi National Accelerator Laboratory, the University of Illinois at Urbana-Champaign, the Institut de Ciències de l’Espai (IEEC/CSIC), the Institut de Física d’Altes Energies, Lawrence Berkeley National Laboratory, the Ludwig Maximilians Universität München and the associated Excellence Cluster Universe, the University of Michigan, NSF’s NOIRLab, the University of Nottingham, the Ohio State University, the University of Pennsylvania, the University of Portsmouth, SLAC National Accelerator Laboratory, Stanford University, the University of Sussex, and Texas A&M University.

BASS is a key project of the Telescope Access Program (TAP),

which has been funded by the National Astronomical Observatories of China, the Chinese Academy of Sciences (the Strategic Priority Research Program “The Emergence of Cosmological Structures” Grant # XDB09000000), and the Special Fund for Astronomy from the Ministry of Finance. The BASS is also supported by the External Cooperation Program of Chinese Academy of Sciences (Grant # 114A11KYSB20160057), and Chinese National Natural Science Foundation (Grant # 11433005).

The Legacy Survey team makes use of data products from the Near-Earth Object Wide-field Infrared Survey Explorer (NEOWISE), which is a project of the Jet Propulsion Laboratory/California Institute of Technology. NEOWISE is funded by the National Aeronautics and Space Administration.

The Legacy Surveys imaging of the DESI footprint is supported by the Director, Office of Science, Office of High Energy Physics of the U.S. Department of Energy under Contract No. DE-AC02-05CH1123, by the National Energy Research Scientific Computing Center, a DOE Office of Science User Facility under the same contract; and by the U.S. National Science Foundation, Division of Astronomical Sciences under Contract No. AST-0950945 to NOAO.

## REFERENCES

- Abazajian K. N., et al., 2009, *The Astrophysical Journal Supplement Series*, 182, 543
- Amiaux J., et al., 2012, in Clampin M. C., Fazio G. G., MacEwen H. A., Oschmann Jacobus M. J., eds, *Society of Photo-Optical Instrumentation Engineers (SPIE) Conference Series Vol. 8442, Space Telescopes and Instrumentation 2012: Optical, Infrared, and Millimeter Wave*. p. 84420Z ([arXiv:1209.2228](https://arxiv.org/abs/1209.2228)), doi:10.1117/12.926513
- Arcelin B., Doux C., Aubourg E., Roucelle C., LSST Dark Energy Science Collaboration 2021, *MNRAS*, 500, 531
- Arora N., Fossati M., Fontanot F., Hirschmann M., Wilman D. J., 2019, *MNRAS*, 489, 1606
- Bahdanau D., Cho K., Bengio Y., 2014, CoRR, [abs/1409.0473](https://arxiv.org/abs/1409.0473)
- Bower R. G., Benson A. J., Malbon R., Helly J. C., Frenk C. S., Baugh C. M., Cole S., Lacey C. G., 2006, *MNRAS*, 370, 645
- Bretonnière H., et al., 2021, arXiv e-prints, [p. arXiv:2105.12149](https://arxiv.org/abs/2105.12149)
- Buncher B., Sharma A. N., Carrasco Kind M., 2021, *MNRAS*, 503, 777
- Camps P., Trayford J. W., Baes M., Theuns T., Schaller M., Schaye J., 2016, *MNRAS*, 462, 1057
- Cheng J., Dong L., Lapata M., 2016, CoRR, [abs/1601.06733](https://arxiv.org/abs/1601.06733)
- Cohen J., 1988, *Statistical Power Analysis for the Behavioral Sciences*. Lawrence Erlbaum Associates
- Cole S., Lacey C. G., Baugh C. M., Frenk C. S., 2000, *MNRAS*, 319, 168
- Croton D. J., et al., 2006, *MNRAS*, 365, 11
- Dewdney P. E., Hall P. J., Schilizzi R. T., Lazio T. J. L. W., 2009, *IEEE Proceedings*, 97, 1482
- Dey A., et al., 2019, *AJ*, 157, 168
- Dhariwal P., Nichol A., 2021, CoRR, [abs/2105.05233](https://arxiv.org/abs/2105.05233)
- Dowson D., Landau B., 1982, *Journal of Multivariate Analysis*, 12, 450
- Dubois Y., et al., 2014, *MNRAS*, 444, 1453
- Fussell L., Moews B., 2019, *MNRAS*, 485, 3203
- Goodfellow I., Pouget-Abadie J., Mirza M., Xu B., Warde-Farley D., Ozair S., Courville A., Bengio Y., 2014, in Ghahramani Z., Welling M., Cortes C., Lawrence N., Weinberger K. Q., eds, Vol. 27, *Advances in Neural Information Processing Systems*. Curran Associates, Inc., <https://proceedings.neurips.cc/paper/2014/file/5ca3e9b122f61f8f06494c97b1afccf3-Paper.pdf>
- He K., Zhang X., Ren S., Sun J., 2015, CoRR, [abs/1512.03385](https://arxiv.org/abs/1512.03385)
- Heusel M., Ramsauer H., Unterthiner T., Nessler B., Hochreiter S., 2017, in Guyon I., Luxburg U. V., Bengio S., Wallach H., Fergus R., Vishwanathan S., Garnett R., eds, Vol. 30, *Advances in Neural Information Processing Systems*. Curran Associates, Inc., <https://proceedings.neurips.cc/paper/2017/file/8a1d694707eb0fe65871369074926d-Paper.pdf>
- Ho J., Jain A., Abbeel P., 2020, in Larochelle H., Ranzato M., Hadsell R., Balcan M. F., Lin H., eds, Vol. 33, *Advances in Neural Information Processing Systems*. Curran Associates, Inc., pp 6840–6851
- Ivezić Ž., et al., 2019, *ApJ*, 873, 111
- Jayaram V., Thickstun J., 2020, CoRR, [abs/2002.07942](https://arxiv.org/abs/2002.07942)
- Jolicoeur-Martineau A., Piché-Taillefer R., des Combes R. T., Mitliagkas I., 2020, CoRR, [abs/2009.05475](https://arxiv.org/abs/2009.05475)
- Jolicoeur-Martineau A., Li K., Piché-Taillefer R., Kachman T., Mitliagkas I., 2021, CoRR, [abs/2105.14080](https://arxiv.org/abs/2105.14080)
- Kadhodaie Z., Simoncelli E. P., 2020, CoRR, [abs/2007.13640](https://arxiv.org/abs/2007.13640)
- Kaviraj S., et al., 2017, *MNRAS*, 467, 4739
- Khandai N., Di Matteo T., Croft R., Wilkins S., Feng Y., Tucker E., DeGraf C., Liu M.-S., 2015, *MNRAS*, 450, 1349
- Kingma D. P., Ba J., 2015, in Bengio Y., LeCun Y., eds, 3rd International Conference on Learning Representations, ICLR 2015, San Diego, CA, USA, May 7-9, 2015, Conference Track Proceedings. [http://arxiv.org/abs/1412.6980](https://arxiv.org/abs/1412.6980)
- Kingma D. P., Welling M., 2014, in Bengio Y., LeCun Y., eds, 2nd International Conference on Learning Representations, ICLR 2014, Banff, AB, Canada, April 14-16, 2014, Conference Track Proceedings. [http://arxiv.org/abs/1312.6114](https://arxiv.org/abs/1312.6114)
- Kocifaj M., Kundracik F., Barentine J. C., Bará S., 2021, *MNRAS*, 504, L40
- Lacoste A., Luccioni A., Schmidt V., Dandres T., 2019, CoRR, [abs/1910.09700](https://arxiv.org/abs/1910.09700)
- Lagos C. d. P., et al., 2019, *MNRAS*, 489, 4196
- Lanusse F., Mandelbaum R., Ravanbakhsh S., Li C.-L., Freeman P., Póczos B., 2021, *MNRAS*, 504, 5543
- Lloyd S., 1982, *IEEE Transactions on Information Theory*, 28, 129
- Lovell C. C., Geach J. E., Davé R., Narayanan D., Li Q., 2021, *MNRAS*, 502, 772
- Misra D., 2019, CoRR, [abs/1908.08681](https://arxiv.org/abs/1908.08681)
- Mustafa M., Bard D., Bhimji W., Lukić Z., Al-Rfou R., Kratochvil J. M., 2019, *Computational Astrophysics and Cosmology*, 6, 1
- Nichol A., Dhariwal P., 2021, CoRR, [abs/2102.09672](https://arxiv.org/abs/2102.09672)
- Paszke A., et al., 2019, in Wallach H., Larochelle H., Beygelzimer A., d'Alché-Buc F., Fox E., Garnett R., eds, *Advances in Neural Information Processing Systems 32*. Curran Associates, Inc., pp 8024–8035. [http://papers.neurips.cc/paper/9015-pytorch-an-imperative-style-high-performance-deep-learning-library.pdf](https://papers.neurips.cc/paper/9015-pytorch-an-imperative-style-high-performance-deep-learning-library.pdf)
- Preechakul K., Chatthee N., Wizadwongsa S., Suwajanakorn S., 2021, CoRR, [abs/2111.15640](https://arxiv.org/abs/2111.15640)
- Ravanbakhsh S., Lanusse F., Mandelbaum R., Schneider J., Póczos B., 2016, arXiv e-prints, [p. arXiv:1609.05796](https://arxiv.org/abs/1609.05796)
- Reiman D. M., Göhre B. E., 2019, *MNRAS*, 485, 2617
- Remy B., Lanusse F., Ramzi Z., Liu J., Jeffrey N., Starck J.-L., 2020, arXiv e-prints, [p. arXiv:2011.08271](https://arxiv.org/abs/2011.08271)
- Rezende D. J., Mohamed S., 2015, in Proceedings of the 32nd International Conference on International Conference on Machine Learning - Volume 37. ICML'15. JMLR.org, p. 1530–1538
- Ronneberger O., Fischer P., Brox T., 2015, in Navab N., Hornegger J., III W. M. W., Frangi A. F., eds, *Lecture Notes in Computer Science Vol. 9351, Medical Image Computing and Computer-Assisted Intervention - MICCAI 2015 - 18th International Conference Munich, Germany, October 5 - 9, 2015, Proceedings, Part III*. Springer, pp 234–241, doi:10.1007/978-3-319-24574-4\_28, [https://doi.org/10.1007/978-3-319-24574-4\\_28](https://doi.org/10.1007/978-3-319-24574-4_28)
- Saharia C., Chan W., Chang H., Lee C. A., Ho J., Salimans T., Fleet D. J., Norouzi M., 2021, CoRR, [abs/2111.05826](https://arxiv.org/abs/2111.05826)
- Salimans T., Karpathy A., Chen X., Kingma D. P., 2017, in 5th International Conference on Learning Representations, ICLR 2017, Toulon, France, April 24-26, 2017, Conference Track Proceedings. OpenReview.net, <https://openreview.net/forum?id=BJrFC6ceg>
- Sasaki H., Willcocks C. G., Breckon T. P., 2021, CoRR, [abs/2104.05358](https://arxiv.org/abs/2104.05358)
- Schawinski K., Zhang C., Zhang H., Fowler L., Santhanam G. K., 2017, *MNRAS*, 467, L110
- Schaye J., et al., 2015, *MNRAS*, 446, 521

- Seitzer M., 2020, pytorch-fid: FID Score for PyTorch, <https://github.com/mseitzer/pytorch-fid>
- Smith M. J., Geach J. E., 2019, *MNRAS*, **490**, 4985
- Sohl-Dickstein J., Weiss E., Maheswaranathan N., Ganguli S., 2015, in Bach F., Blei D., eds, Proceedings of Machine Learning Research Vol. 37, Proceedings of the 32nd International Conference on Machine Learning. PMLR, Lille, France, pp 2256–2265, <http://proceedings.mlr.press/v37/sohl-dickstein15.html>
- Somerville R. S., Primack J. R., 1999, *MNRAS*, **310**, 1087
- Song Y., Ermon S., 2019, in Wallach H., Larochelle H., Beygelzimer A., d'Alché-Buc F., Fox E., Garnett R., eds, Vol. 32, Advances in Neural Information Processing Systems. Curran Associates, Inc., <https://proceedings.neurips.cc/paper/2019/file/3001ef257407d5a371a96dcd947c7d93-Paper.pdf>
- Song Y., Ermon S., 2020, in Larochelle H., Ranzato M., Hadsell R., Balcan M. F., Lin H., eds, Vol. 33, Advances in Neural Information Processing Systems. Curran Associates, Inc., pp 12438–12448, <https://proceedings.neurips.cc/paper/2020/file/92c3b916311a5517d9290576e3ea37ad-Paper.pdf>
- Song Y., Sohl-Dickstein J., Kingma D. P., Kumar A., Ermon S., Poole B., 2021, in International Conference on Learning Representations. <https://openreview.net/forum?id=PXTIG12RRHS>
- Spindler A., Geach J. E., Smith M. J., 2021, *MNRAS*, **502**, 985
- Srivastava R. K., Greff K., Schmidhuber J., 2015, CoRR, abs/1505.00387
- Stark D., et al., 2018, *MNRAS*, **477**, 2513
- Stone C., Courteau S., 2019, *ApJ*, **882**, 6
- Stone C., Courteau S., Arora N., 2021, *ApJ*, **912**, 41
- Strubell E., Ganesh A., McCallum A., 2019, in Proceedings of ACL 57. Association for Computational Linguistics, Florence, Italy, p. 3645, [doi:10.18653/v1/P19-1355](https://doi.org/10.18653/v1/P19-1355)
- Szegedy C., Vanhoucke V., Ioffe S., Shlens J., Wojna Z., 2016, in Proceedings of the IEEE Conference on Computer Vision and Pattern Recognition (CVPR).
- Tamosiunas A., Winther H. A., Koyama K., Bacon D. J., Nichol R. C., Mawdsley B., 2020, arXiv e-prints, p. [arXiv:2004.10223](https://arxiv.org/abs/2004.10223)
- Trayford J. W., et al., 2017, *MNRAS*, **470**, 771
- Vincent P., 2011, *Neural Computation*, **23**, 1661–1674
- Vogelsberger M., et al., 2014, *MNRAS*, **444**, 1518
- Wilman D. J., Zibetti S., Budavári T., 2010, *MNRAS*, **406**, 1701
- York D. G., et al., 2000, *AJ*, **120**, 1579

This paper has been typeset from a  $\text{\TeX}/\text{\LaTeX}$  file prepared by the author.